PAPER

Check for updates

Ion–dipole interaction motivated Zn²⁺ pump and anion repulsion interface enable ultrahigh-rate Zn metal anodes†

Song Huang,[a] Rong Tang,[b] Xiaoqing Liu,[a] Yufei Zhang,[a] Yongchao Tang,[a] Zhipeng Wen,[a] Minghui Ye,[a] Yang Yang[*b] and Cheng Chao Li [ID] [*a]

Aqueous Zn–metal batteries are considered promising candidates for next-generation energy storage. However, their reliability, especially under high-rate conditions, is compromised by the poor cycling stability of Zn metal anodes, caused by insufficient Zn²⁺ replenishment owing to concentration gradients at the reaction interface. Herein, we introduce a zinc perfluorovalerate interfacial layer (Zn@PFPA) that serves as a self-expedited Zn²⁺ pump through an *in situ* organic acid etching route. This distinctive feature ensures rapid and dynamic interfacial replenishment of Zn²⁺ to eliminate the concentration gradients, leading to non-dendritic and highly reversible Zn plating/stripping behaviors, even at elevated rates. Theoretical calculations and experimental results highlight the swift Zn²⁺ transport kinetics driven by ion–dipole interactions, maintaining a steady and homogenous Zn²⁺ flux. Moreover, the high electronegativity and hydrophobic properties of the Zn@PFPA layer further enable charge repulsion of detrimental anions and mitigate free water present at the electrode/electrolyte interface, fundamentally inhibiting the HER and by-product generation. Consequently, the Zn@PFPA electrode displays an outstanding cumulative capacity of 95 000 mA h cm⁻² with a lifespan of 1900 h at an exceptionally high current density of 50 mA cm⁻². Furthermore, its feasibility is also demonstrated by coupling with a high-loading I_2 cathode (~9.0 mg cm⁻²) to fabricate pouch batteries, achieving impressive 10 000 stable cycles at 10 A g⁻¹.

Broader context

Aqueous zinc-ion batteries featuring affordability, safety and sustainability have emerged as a promising alternative energy storage technology, especially in large-scale energy storage. Such applications require rapid and high-power responses within limited durations to address the fluctuation of electricity consumption, imposing stringent demands on the high-rate cycling stability of ZIBs. However, under high-rate conditions, the insufficient Zn²⁺ replenishment at the Zn metal anode interface compromises the cycling stability of the whole system because of concentration gradients. Constructing a 3D conductive structure generally reduces localized effective current density, thus relieving the concentration gradients caused by the high-rate current. Nevertheless, such a structure fails to withstand the invasion of the HER, corrosions and H₂O molecules. It is particularly critical to incorporate the designs of interfacial protective layers on zinc substrates with large active areas. Herein, a zinc perfluorovalerate interfacial layer (Zn@PFPA) is introduced through an *in situ* organic acid etching route, which serves as a self-expedited Zn²⁺ ion pump. This unique functionality ensures the dynamic and fast interfacial replenishment of Zn²⁺ ions, resulting in highly reversible Zn plating/stripping behaviors even at high rates. Moreover, the high electronegative and hydrophobic nature of the Zn@PFPA layer also contributes to the charge repulsion of anions and free water at the electrode/electrolyte interface, inhibiting the HER and by-product generation fundamentally. This work provides novel insights for the implementation of practical high-loading zinc–iodine batteries with fast-charging characteristics.

[a] *Guangdong Provincial Key Laboratory of Plant Resources Biorefinery, School of Chemical Engineering and Light Industry, Guangdong University of Technology, Guangzhou 510006, China. E-mail: licc@gdut.edu.cn*

[b] *College of Chemistry and Chemical Engineering, State-Province Joint Engineering Laboratory of Power Source Technology for New Energy Vehicle, State Key Laboratory of Physical Chemistry of Solid Surfaces, Xiamen University, Xiamen 361005, P. R. China. E-mail: yangyang419@xmu.edu.cn*

† Electronic supplementary information (ESI) available. See DOI: https://doi.org/10.1039/d3ee02945j

1. Introduction

Owing to rising safety and sustainability concerns associated with commercial lithium-ion batteries, there is an urgent pursuit towards the development of alternative energy storage technologies.[1–3] Aqueous zinc-ion batteries (ZIBs) stand out due to their cost-efficiency, the utilization of safe aqueous electrolytes, and their commendable intrinsic theoretical capacity.[4,5] It has

This journal is © The Royal Society of Chemistry 2024

Energy Environ. Sci., 2024, **17**, 591–601 | 591

been predicted that the largest potential market for ZIB systems will cater to large-scale energy storage, addressing the variability of electricity consumption.[6,7] Such applications often require rapid and high-power responses within limited durations, imposing stringent demands on the high-rate cycling stability of ZIBs. Unfortunately, Zn metal anodes encounter severe issues including Zn dendrite formation, the H_2 evolution reaction (HER) side reaction, and H_2O-induced self-corrosion, which lowers the Coulombic efficiency and curtails the cycle life of Zn metal anodes.[8–12] It should be noted that these interface-related concerns intensify under high-rate conditions.

At elevated current densities, zinc metal deposition transitions from the traditional reaction control observed at a relatively low current density to a diffusion control type. This signifies that fast Zn^{2+} ion consumption combined with inadequate ionic transport at the electrode/electrolyte interface leads to pronounced concentration gradients and non-uniform Zn^{2+} ion distribution, exacerbating the dendritic growth morphology.[13–16] Furthermore, the heightened Zn deposition overpotential also provides a potential driving force for the HER side reaction, triggering local pH shifts and producing irreversible by-products associated with detrimental anions at the interface.

To suppress Zn dendrite formation and improve the high-rate cycling stability of metallic Zn anodes, one prevailing approach is the construction of three-dimensional (3D) conductive architectures. This design presents a larger active area, which reduces the localized effective current density, thus delaying dendrite formation.[17–22] The hierarchical graphene matrix introduced by Zeng et al. is an example of such a 3D structure that effectively mitigates Zn^{2+} concentration gradients and enables stable Zn plating/stripping behaviors at an extremely high current density of 80 mA cm^{-2}.[17] However, metallic Zn should be electrodeposited into these pre-designed 3D hosts, which is rather complex and hard to be scaled up.[23] Additionally, the high specific surface area of these structures also inevitably creates more active sites for the HER, which hinders their overall effectiveness.[24] Therefore, it is particularly critical to incorporate the designs of interfacial protective layers on zinc substrates with large active areas. These protective layers can modify the electrode/electrolyte interface through mechanisms such as ion diffusion channel tunning, chemical adsorption, and electrostatic field establishment.[25] The components of the interface are directly manipulated through different heterogeneous species to influence the local ionic behaviour in the electrolyte, which effectively modulates the desolvation process, corrosions and the HER at the interface. Furthermore, by influencing the distribution of Zn^{2+} ion flux, these protective layers can effectively promote uniform Zn deposition morphology. The spatial screening effect provided by the interfacial protective layer also prevents direct contact between the electrolyte and the Zn electrode, thus reducing side reactions. Nevertheless, these reported interfacial modification strategies often fail to promptly replenish Zn^{2+} ions during rapid Zn deposition owing to the additional electrochemical polarization induced by the additional coating layer, resulting in limited improvements under high-rate cycling conditions.

Thus, realizing a Zn plating/stripping behaviour that boasts enhanced electrochemical reaction kinetics remains a formidable challenge in optimizing high-rate ZIB applications.

Herein, dynamic and rapid Zn^{2+} ion replenishment at the interface is realized by using a zinc perfluorovalerate (Zn@PFPA) functional layer acting as a self-expedited Zn^{2+} ion pump, essentially inhibiting Zn dendrite formation and side reactions at high current densities. The Zn@PFPA layer is fabricated on the surface of the metallic Zn anode through an in situ organic acid etching route, affording excellent adhesive strength and an etching pattern with high Zn^{2+}-ion flux. Due to the significant electronegativity difference of the C–F bond, the terminal F atom accumulates a substantial negative charge, engendering strong ion–dipole interactions with positively charged Zn^{2+} ions. Benefitting from the fast Zn^{2+} transport kinetics motivated by ion–dipole interactions, a continuous and rapid Zn^{2+} ion transport network is formed, bridging the Zn reduction reaction interface and the bulk electrolyte. This ensures dynamic maintenance of the interfacial Zn^{2+} ion concentration and eradicates concentration gradients at the interface. Moreover, the high polarity and hydrophobic nature of the Zn@PFPA layer are also beneficial for the charge repulsion of detrimental anions and free water at the electrode/electrolyte interface, restraining the HER and by-product generation fundamentally. This work is expected to provide novel insights for the implementation of practical high-loading of zinc–iodine batteries with fast-charging characteristics.

2. Results and discussion

In aqueous electrolytes, Zn^{2+} ions tend to interact with H_2O, forming hydrated species ($Zn(H_2O)_6^{2+}$). Its deposition process at the electrode/electrolyte interface primarily involves two stages: the desolvation of $Zn(H_2O)_6^{2+}$ to produce Zn^{2+} ions followed by the reduction of Zn^{2+} to its metallic form.[26] Given the significant energy barriers associated with the desolvation of hydrated Zn^{2+}, this step often becomes the rate-limiting factor in the deposition process.[27,28] A key consideration in enhancing the Zn^{2+} ion diffusion and influencing the solvation structure involves leveraging the induced dipole moments between Zn^{2+} and heteroatoms in organic functional groups of the in-built interface. Notably, a direct relationship exists between the induced dipole moment and the electronegativity difference (ΔEN); a larger ΔEN results in a stronger dipole, making it easier for Zn^{2+} to shed its surrounding H_2O molecules.[29] From calculations involving heteroatoms bonded to carbon (Fig. 1a), it is evident that the C–F bond stands out, primarily because of fluorine's exceptionally high electronegativity. Based on the molecule level considerations, perfluoropentanoic acid (PFPA) with multiple C–F bonds has been applied to the metallic Zn surface. This treatment leads to the in situ etching and formation of a Zn@PFPA layer, subsequently fostering a high Zn^{2+} flux pattern (Fig. 1c). The formation of such a distinctive pattern is intimately associated with the strong repulsive forces among PFPA molecules surrounded by the C–F bond with a high dipole moment. These repulsive
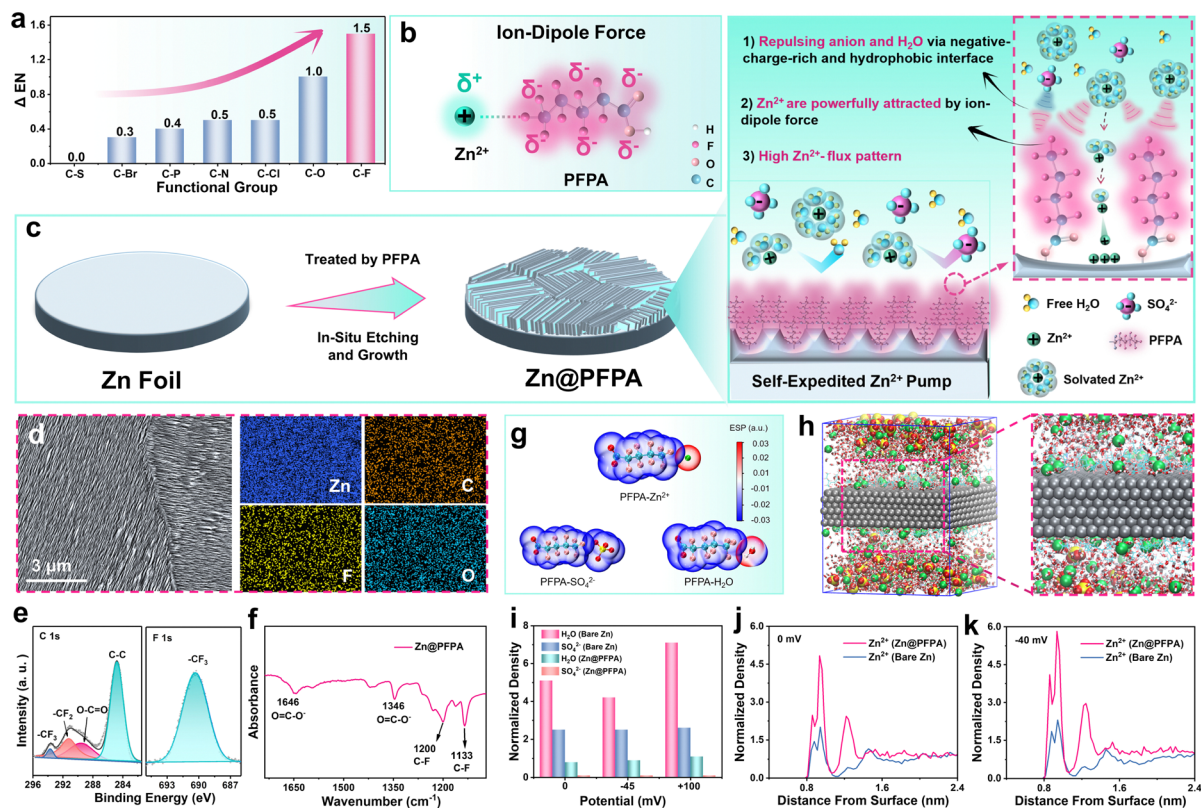
Fig. 1 Construction of a self-expedited Zn^{2+} pump by PFPA molecules. (a) The ΔEN of diverse organic bonds. (b) The schematic diagram of the Zn^{2+}-dipole force. (c) The schematic diagram of construction *in situ* of Zn@PFPA. The inset on the right is the negative charge interface and its effect on different species. (d) SEM and the corresponding elemental mapping images of Zn@PFPA. (e) High-resolution C 1s and F 1s spectra of Zn@PFPA. (f) FT-IR of the Zn@PFPA. (g) ESP between the PFPA and Zn^{2+}, SO_4^{2-} and H_2O, respectively. (h) The snapshot of the Zn@PFPA interface obtained using MD simulation. (i) Comparison of the normalized density of SO_4^{2-} and H_2O on bare Zn and Zn@PFPA surfaces at different potentials (j) and (k). Normalized density curves of Zn^{2+} on bare Zn and Zn@PFPA surfaces at different potentials.

forces preclude the PFPA from being tightly aligned on the zinc metal surface, ultimately resulting in a regular linear concave–convex pattern. The color of the metallic Zn surface changes from metallic silver to white after treatment, and the modified Zn@PFPA surface can withstand mechanical stresses such as curling, folding, and adhesive tape tearing, showcasing its durable stability (Fig. S1a and S2, ESI†). The cross-sectional morphology of Zn@PFPA after acid etching is exhibited in Fig. S3, ESI.† The regular etching pattern can be clearly observed and presents a large surface area.

The underlying mechanism involves the carboxyl group from the treating agent reacting with metallic Zn, leading to the formation of a zinc perfluorovalerate molecular layer. This new layer becomes rich in negative charges, attributed to the high electronegativity difference (ΔEN) inherent to the C–F bond. As a consequence, a potent Zn^{2+}-dipole force forms near the surface, facilitating Zn^{2+} attraction, thereby enhancing its diffusion and desolvation (Fig. 1b). Meanwhile, this negative charge-rich layer repels anions and water molecules effectively, minimizing potential corrosion and the HER. Besides, the rough surface of bare Zn is substituted by the regular and highly active areal pattern after etching (Fig. 1d and Fig. S1b, ESI†) which efficiently decreases the local current density.

Such a regular pattern cooperating with the negative-charge-rich interface constitutes a self-accelerating Zn^{2+} pump that dynamically replenishes the Zn^{2+} for the electrode/electrolyte interface at high rates. The corresponding elemental mapping in SEM images reveals the uniform distribution of Zn, C, F and O elements, confirming the presence of PFPA molecule chains on the surface of the etching layer (Fig. 1d). Detailed chemical environment characterization using high-resolution X-ray photoelectron spectroscopy (XPS) has been depicted in Fig. 1e. Four peaks located at the 293.7, 291.2, 289.6 and 284.8 eV are associated with the $-CF_3$, $-CF_2$, $O-C{=}O$ and C–C bonds in the C 1s spectrum, respectively, further confirming the presence of the PFPA molecule chains on the Zn anode surface.[30,31] And the peak located to 690.4 eV belongs to the $-CF_3$ bond in the F 1s spectrum.[32] Further validation is conducted on the Fourier-transform infrared (FTIR) spectroscopy, as shown in Fig. 1f. Vibration peaks at 1646 and 1346 cm^{-1} correspond to the asymmetric stretching and symmetric stretches of the $O{=}C-O^-$ group in PFPA. The presence of the C–F bond stretches at 1200 and 1133 cm^{-1} further corroborates the successful integration of PFPA on metallic Zn.[33] X-ray diffraction was carried out to confirm the existence of PFPA as an organic molecule chain and not as other crystallization products on the metallic

This journal is © The Royal Society of Chemistry 2024

Energy Environ. Sci., 2024, **17**, 591–601 | **593**

Zn surface (Fig. S4, ESI†). Evidently, no other signal peaks were detected except for the characteristic peaks of the metal Zn.

In order to illustrate the negative-charge-rich interfaces constructed *via* the PFPA molecule and to understand its effects on the ion distribution near the anode surface, theoretical calculations were conducted. The electrostatic potential (ESP) of PFPA interacting with other species in the electrolyte is depicted Fig. 1g. The high ΔEN of the C–F bond leads to a surrounding negative charge layer around the PFPA molecule, which attracts the positively charged Zn^{2+} *via* the Zn^{2+}-dipole force, enhancing ion transport at the interface. In contrast, SO_4^{2-} anions experience repulsion from the PFPA molecule, significantly reducing the possibility of forming the undesired by-product of $Zn_4SO_4(OH)_6 \cdot nH_2O$ (dead zinc).[34] It is worth noting that the polar H_2O molecule also possesses the opposite-charge terminal (O and H) and the lone pair electrons on the F atom might generate a H bond with H_2O. However, the contact angle measurement (Fig. S5, ESI†) revealed that the Zn@PFPA interface exhibits a hydrophobic characteristic with a larger angle of 114° compared to that of bare Zn (87°). This suggests a dominant repulsion between the F and O atoms, overshadowing the attraction between F and H atoms, reducing the free H_2O molecule at the interface to curb the HER.

To gain insights into the behaviour of various species, molecular dynamics (MD) simulations focusing on the Zn@PFPA interface were carried out. A snapshot at 0 mV is shown in Fig. 1h. Near the surface of the Zn anode, the amounts of SO_4^{2-} and H_2O are diminished compared to the bulk electrolyte, aligning with the observations from the electrostatic potential and contact angle analyses. For a more quantitative understanding, normalized density variations based on distance from the surface are obtained (Fig. 1i and Fig. S6, ESI†). During the simulation, three potential biases were set on the Zn@PFPA interface to replicate different states: PZC (0 mV), deposition (-40 mV), and stripping ($+100$ mV). Notably, even under a favorable overpotential of $+100$ mV, the SO_4^{2-} near the Zn@PFPA surface was nearly eradicated, holding a normalized density of just 0.1. This suggests that the accumulated negative charge at the Zn@PFPA interface produces a repulsion potent enough to counter the coulombic attraction between SO_4^{2-} and the Zn anode.[35] Conversely, on the unmodified Zn surface, SO_4^{2-} maintains a high content across all biases, thereby perpetuating the formation of dead Zn. Simultaneously, the identical trend appears in the H_2O molecule that a normalized density of *ca.* 1 on the Zn@PFPA surface is considerably lower than that of bare Zn. Interestingly, the Zn^{2+} in the biases of -40 mV (deposition state) present an evident higher normalized density than that of 0 mV, suggesting the Zn@PFPA interface generates a self-expedited-pump effect to accelerate the replenishment of Zn^{2+} to the interface (Fig. 1j and k). As an obvious comparison, however, the Zn^{2+} ion concentration on bare Zn remains almost consistent across different biases.

The electrochemical performance is assessed by symmetric batteries assembled by the Zn@PFPA electrode. A moderate current density of 5 mA cm^{-2} with an areal capacity of 1 mA h cm^{-2} is illustrated in Fig. 2a. Benefiting from the negative-charge interface that repels SO_4^{2-} and H_2O molecules and the optimized electric field, the Zn@PFPA electrode achieves an exceptional lifespan exceeding 2800 h. In comparison, the untreated Zn exhibits a short circuit after merely 102 h, likely due to aggressive dendrite growth and uncontrolled HER. The current densities were progressively ramped up from 1 to 50 mA cm^{-2} to validate the superior ion transport kinetics of the Zn@PFPA interface (Fig. 2b) and the comparative data on polarization potential is shown in Fig. 2c and Fig. S7, ESI.† Since slow ionic conduction is required at a low rate, few differences between the bare Zn and Zn@PFPA electrode in polarization potential appear at the 1, 2 and 5 mA cm^{-2}. At lower rates (1, 2, and 5 mA cm^{-2}), the difference in polarization potential between bare Zn and the Zn@PFPA electrode is marginal. However, as the rate increases, the polarization voltage for the untreated zinc escalates significantly, whereas the Zn@PFPA shows a subdued rise. At the peak current density of 50 mA cm^{-2}, the Zn@PFPA electrode delivers a small polarization voltage of 147 mV, a value 2.6 times less than that of bare Zn (392 mV). The distinct difference is attributed to the self-expedited pump to accelerate the process from desolvation to deposition of hydrated Zn^{2+}. Cyclic voltammetry (CV) curves reinforce this conclusion, with Zn@PFPA showcasing a smaller voltage difference between redox peaks and a larger area, indicating rapid ion transport kinetics and increased active sites (Fig. S8, ESI†). The cycling life in harsher conditions is investigated at the extremely high current density of 50 mA cm^{-2} to exert the potential of Zn@PFPA. As revealed in Fig. 2d, the Zn@PFPA electrode endures a record-breaking lifespan of over 1900 h, corresponding to the unprecedented cumulative capacity of 95 000 mA h cm^{-2}, while the bare Zn appears short circuit only in the 31 h. Therefore, even in high-rate extreme condition, the Zn@PFPA still maintain the unique function of fast Zn^{2+} replenishment propelled by the self-expedited pump to ensure continuous and homogeneous Zn^{2+} flux. Additionally, the hindrance of anion and interfacial H_2O by negative-charge PFPA is another vital contributor to its impressive lifespan.

The Cu@PFPA||Zn half batteries are assembled to investigate the platting/stripping reversibility of Zn^{2+} for the zinc perfluorovalerate layer. The synthesized details of the Cu@PFPA electrode are shown in the experiment section and Fig. S9, ESI.† As shown in Fig. 2e, profiting from the alleviative concentration gradient that affords a homogeneous Zn^{2+} environment, the Cu@PFPA||Zn battery achieves high reversible plating/stripping of 1650 cycles with the excellent average coulombic efficiency (CE) of 99.8% at the 10 mA cm^{-2} in an areal capacity of 1 mA h cm^{-2}. However, the Cu||bare Zn battery fails at *ca.* 800 cycles and presents a remarkable fluctuation of CE during cycling owing to the continuous accumulation of dead Zn. Simultaneously, the polarization potential is studied based on the assembled half batteries to confirm the ultrafast Zn^{2+} replenishment interface of the zinc perfluorovalerate layer (Fig. 2f). The restricted ion kinetics make the Cu||bare Zn battery suffer from higher polarization voltages of 129.7 mV than that of Cu@PFPA||Zn battery (103.0 mV). With the increase of cycles, what's worse, the polarization voltages of
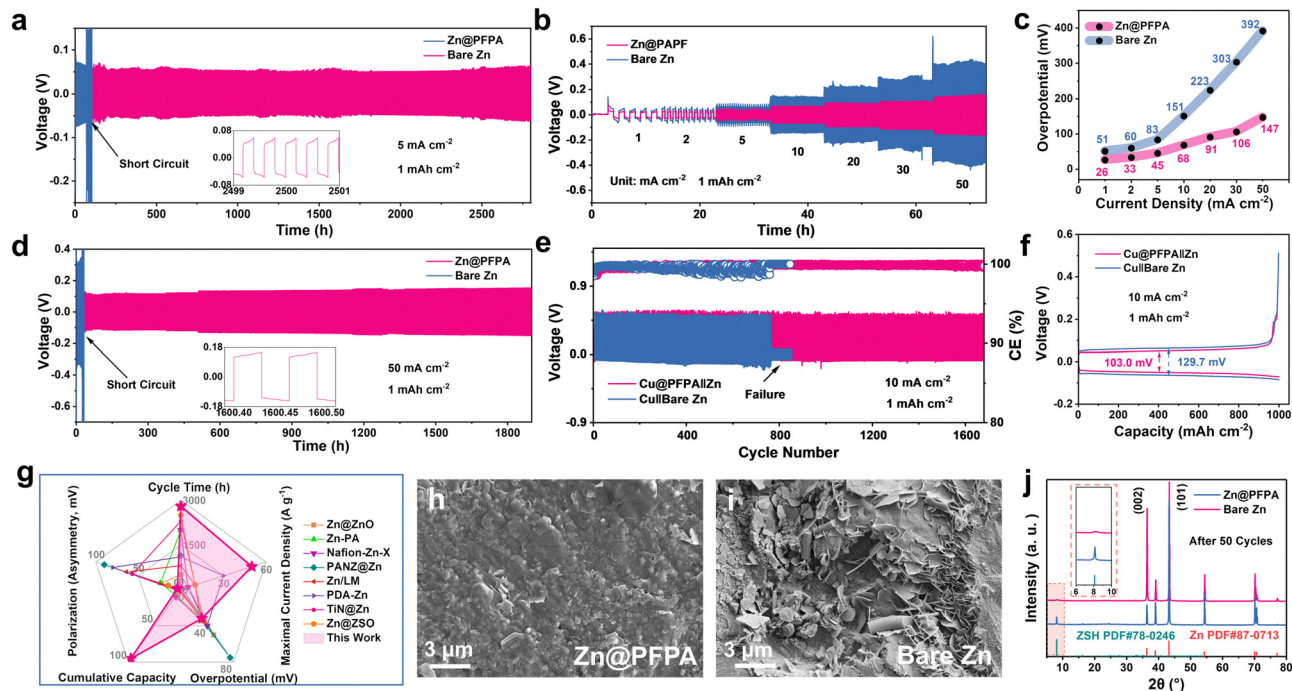
594 | *Energy Environ. Sci.*, 2024, **17**, 591–601

This journal is © The Royal Society of Chemistry 2024

Fig. 2 The electrochemical performance of symmetric and asymmetric batteries for bare Zn and Zn@PFPA. (a) The symmetric batteries at 5 mA cm^{-2} and 1 mA h cm^{-2}. (b) Rate performance at various current densities. (c) Overpotential at different current densities based on the rate performance. (d) The symmetric batteries of long-term cycles at a high current density of 50 mA cm^{-2}. (e) The half batteries are at 10 mA cm^{-2} and 1 mA h cm^{-2}. (f) Voltage profiles of half batteries at 10 mA cm^{-2} and 1 mA h cm^{-2}. (g) The comparison with the previously published literature in terms of cycle time, maximal current density, overpotential, cumulative capacity and polarization (asymmetric batteries). (h) and (i) SEM images of Zn@PFPA (h) and bare Zn (i) after cycling. (j) XRD patterns of Zn@PFPA and bare Zn after cycling.

bare Zn gradually elevate due to the continuous generation of by-products. In contrast, Zn@PFPA maintains a durable polarization voltage even after 800 cycles (Fig. S10, ESI†). These desired performances in Zn@PFPA electrode further are compared with the literature previously published in terms of cycling time, maximal current density, overpotential, cumulative capacity and polarization voltage (asymmetric batteries) exhibited in Fig. 2g.[11,36–42] Evidently, various indexes present an advantage site and even far ahead, manifesting the effectiveness of such elaborate interface. The SEM images of the electrode after cycling are revealed in Fig. 2h and i. The flat surface on the Zn@PFPA electrode is observed and the Zn deposits on it by the morphology of the hexagonal plane, while the bare Zn forms irregular dendrites and drastic corrosion that corresponds to its cycling life. The surficial component is further assessed by the XRD. The standard peak associated with the by-product of basic zinc sulfate (ZSH) is detected at *ca.* 8.1° for the bare Zn but is absent for the Zn@PFPA. These results confirm the efficient suppression of dendrites and corrosion.

To clarify the influence of the PFPA interface on the desolvation process of Zn^{2+} and understand how the entire Zn^{2+} replenishment process works, more in-depth theoretical calculation is carried out. Firstly, the adsorption effect for Zn ion on the bare Zn and Zn@PFPA substrates is quantified by the adsorption energy calculation. The corresponding adsorption configuration of bare Zn and Zn@PFPA interface based on the

Zn (010) plane are displayed in Fig. 3a and b. As expected, the PFPA with negative-charge F terminal generates additional attraction toward Zn ion with a more favorable adsorption energy of −1.14 eV than that of bare Zn (−0.78 eV). The increased attraction propels the hydrated Zn^{2+} to accelerate to approach the PFPA molecule, thus achieving fast Zn^{2+} replenishment near the surface. Moreover, compared with the bare Zn, a higher Zn^{2+} concentration on the Zn@PFPA interface also is confirmed by COMSOL simulations of concentration distribution for Zn ion, which affords adequate and continuous Zn^{2+} fluxes for high reversible cycling at a high rate (Fig. S11, ESI†). In addition to the absorption energy, the potential energy also is employed to clarify the interaction between heteroatoms or molecules. The potential energy of PFPA with Zn^{2+} and SO$_4^{2-}$ varies with the distance (*d*) between them exhibited in Fig. 3c. When *d* is located at the 3.64 angstrom, the potential energy reaches a maximum between the PFPA and Zn ions, in which PFPA exerts a strong ionic dipole force on the Zn ion to promote the rapid approach to the interface. With the increase of distance, the potential energy of Zn^{2+} gradually converges but retains a value even at 20 angstroms, indicating that the PFPA interface can generate an ion–dipole force large enough to impact a large range of zinc ions. This range effect effectively eliminates the Zn^{2+} concentration gradient brought at the high current density. On the contrary, the SO$_4^{2-}$ appears as a positive potential energy with the rise of *d*, which manifests it is repulsed from the negative-charge-rich PFPA interface,
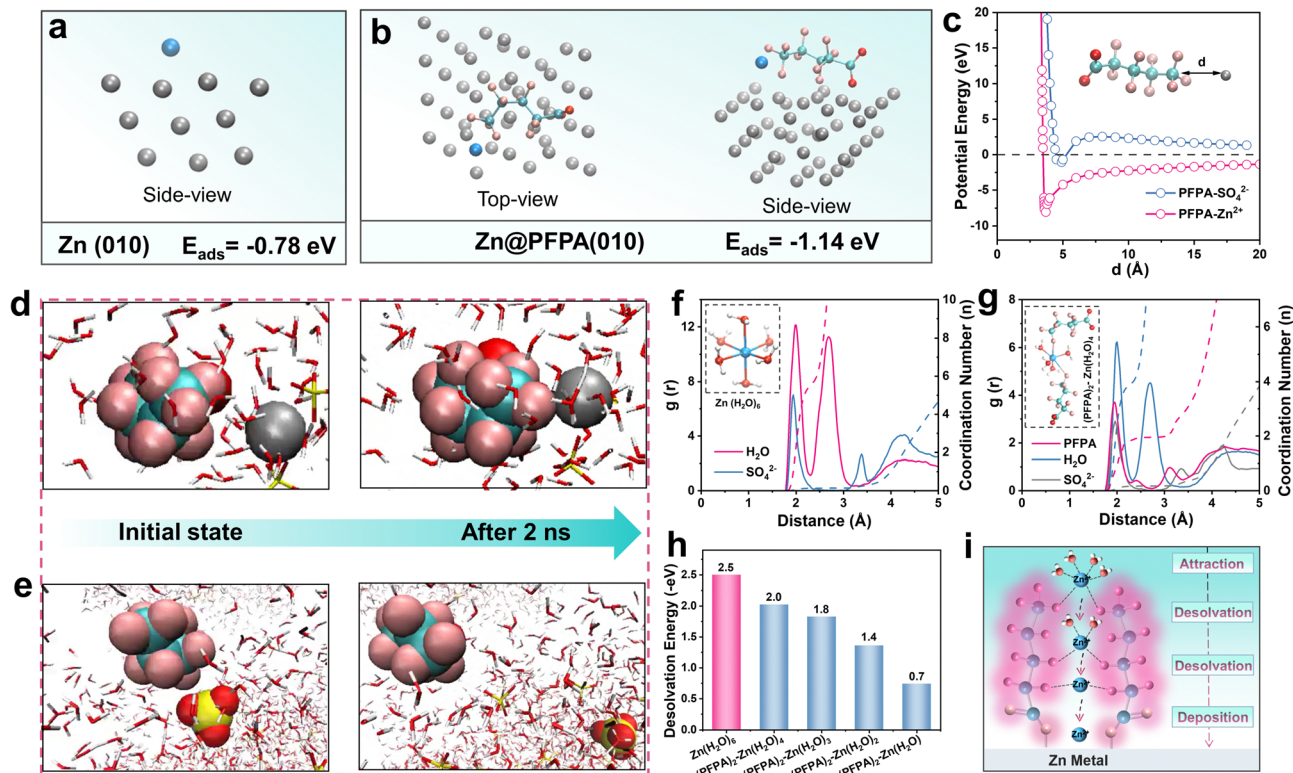
This journal is © The Royal Society of Chemistry 2024

Energy Environ. Sci., 2024, **17**, 591–601 | **595**

Fig. 3 The PFPA actuates ultrafast desolvation of hydrated Zn^{2+}. (a) and (b) The adsorption configuration of the Zn atom on the Zn (010) plane (a) and Zn@PFPA surface (b). (c) The potential energy of PFPA interacts with Zn^{2+} and SO_4^{2-}, respectively, which is obtained from quantum chemistry calculation. (d) and (e) Structural snapshots from MD concerning the interaction of PFPA with Zn ion (d) and SO_4^{2-} (e). (f) and (g) RDFs and corresponding coordination numbers of different species with the Zn ion solvation sheath in bare Zn (f) and Zn@PFPA (g). (h) The calculated desolvation energy barriers on bare Zn and Zn@PFPA interfaces. (i) The complete desolvation process impacted by the PFPA interface of the Zn@PFPA electrode.

corresponding to the result of MD simulation. The dynamic configuration concerning the interaction of PFPA with other species is derived to visualize the track between them. As exhibited in Fig. 3d, when Zn ions diffuse from the electrolyte to the nearby area of PFPA, after 2 ns, the Zn cations are spontaneously attracted to the PFPA surface to combine with the negative-charge F terminal. In this process, the PFPA molecules function as a self-expedited Zn^{2+} pump and display the dynamic Zn^{2+} replenishment. Simultaneously, once the SO_4^{2-} anion approaches the PFPA molecule, a repulsive force excludes it from the interface, intercepting the formation path of dead Zn on the interface (Fig. 3e).[13]

Given the large binding force of PFPA with the Zn ion, the radial distribution function (RDF) then is obtained by the MD simulation to elucidate how the solvation structure is affected by the PFPA molecules. In the normal surface of bare Zn, the coordination number of H_2O in the Zn^{2+} solvation shell is calculated as about 6, corresponding to the well-known structure of hydrated Zn ion, *i.e.*, $Zn^{2+}(H_2O)_6$ (Fig. 3f).[43] Interestingly, due to the strong attraction to the Zn^{2+} on the Zn@PFPA interface, two the PFPA molecules substitute two H_2O to participate in the solvation shell and form a new solvation structure of $(PFPA)_2-Zn^{2+}(H_2O)_4$ (Fig. 3g). Subsequent desolvation energy barrier calculation demonstrates that the formation of $(PFPA)_2-Zn^{2+}(H_2O)_4$ structure becomes a critical step in

rapid desolvation for the Zn^{2+} because it prominently reduces the desolvation energy barrier of Zn^{2+} compared with the $Zn^{2+}(H_2O)_6$ (Fig. 3h). More importantly, the energy barrier continuously declines with the H_2O detached and finally the $(PFPA)_2-Zn^{2+}(H_2O)$ structure only requires a rather low energy barrier of 0.7. Therefore, the mechanism of the Zn^{2+} replenishment by the self-expedited pump can be clarified and summarized as follows. Firstly, the $Zn^{2+}(H_2O)_6$ near the PFPA molecules is attracted to fast diffuse to the surface and combinate with the F terminal. Then two PFPA molecules exclude two H_2O to form a new solvation structure of $(PFPA)_2-Zn^{2+}(H_2O)_4$ that possesses a smaller desolvation energy barrier than that of $Zn^{2+}(H_2O)_6$, by which the desolvation process is continuously expedited with H_2O detached. The highly active area of the pattern receives a large amount of rapidly transported zinc ions to deposit as zinc metal and thus accomplish an accelerated ion transport process on the interface. Such an expedited process can relieve the Zn^{2+} concentration gradients caused by the fast changed current at a high rate and generate homogeneous Zn^{2+} flux for deposition, resulting in non-dendrites and high reversible stripping/plating. Apart from theoretical calculations, experiments have also been tested to confirm the self-accelerating interfaces. The Zn^{2+} transference number of the interface is shown in Fig. S12, ESI,† the Zn@PFPA obtains a faster ion transference of 0.60 than that of bare Zn (0.26). The rather low

596 | *Energy Environ. Sci.*, 2024, **17**, 591–601

This journal is © The Royal Society of Chemistry 2024

Zn^{2+} transference number of bare Zn is attributed to the hindrance of the hydrated shell and the electrostatic interaction with SO_4^{2-} on the surface. Moreover, the assistance of PFPA for the desolvation of hydrated Zn^{2+} also is verified by the calculation of desolvation activation energy based on the Arrhenius equation (Fig. S13, ESI†).[44] The Zn@PFPA presents an evident low activation energy of 35.5 kJ mol^{-1}, which is consistent with the theoretical calculation results. The bare Zn with the activation energy of 53.6 kJ mol^{-1} reveals that it is difficult to get over the effect from the solvation shell and the electrostatic interaction with SO_4^{2-}.

The ability to suppress HER of the Zn@PFPA electrode is assessed. *In situ* contact angle measurement is carried out to compare hydrophilic and hydrophobic properties on the bare Zn and Zn@PFPA surface shown in Fig. 4a. Attributed to the negative charge interface, the Zn@PFPA exhibits an obtuse angle of 116° at pristine, which is larger than that of bare Zn (87°). While the contact angle decreased over time for both samples, it was significantly faster for bare zinc, eventually reaching 34°. The favorable contact increases the free water at the interface of bare Zn, which provides an advantageous environment for corrosion, side reactions and the HER. As for Zn@PFPA, there is still a large angle of 77° after 10 min, suggesting a relatively hydrophobic property. Generally speaking, severe HER consumes the H$^+$ in the water and the hydroxides left behind raise the pH of the electrolyte, which encourages interfacial corrosion and the formation of dead zinc.[22] To obtain the variety of pH values during the cycling of both electrodes, a cell consisting of a pH meter and a cuvette was constructed, in which the electrolyte is added with only 5 mL (Fig. 4b and Fig. S14a, ESI†). As expected, Zn@PFPA achieves a steadier pH trend during cycling, while bare zinc appears a continuous rise because of the intimate contact of water that conduce to obtain electron and to be reduced to H$_2$.
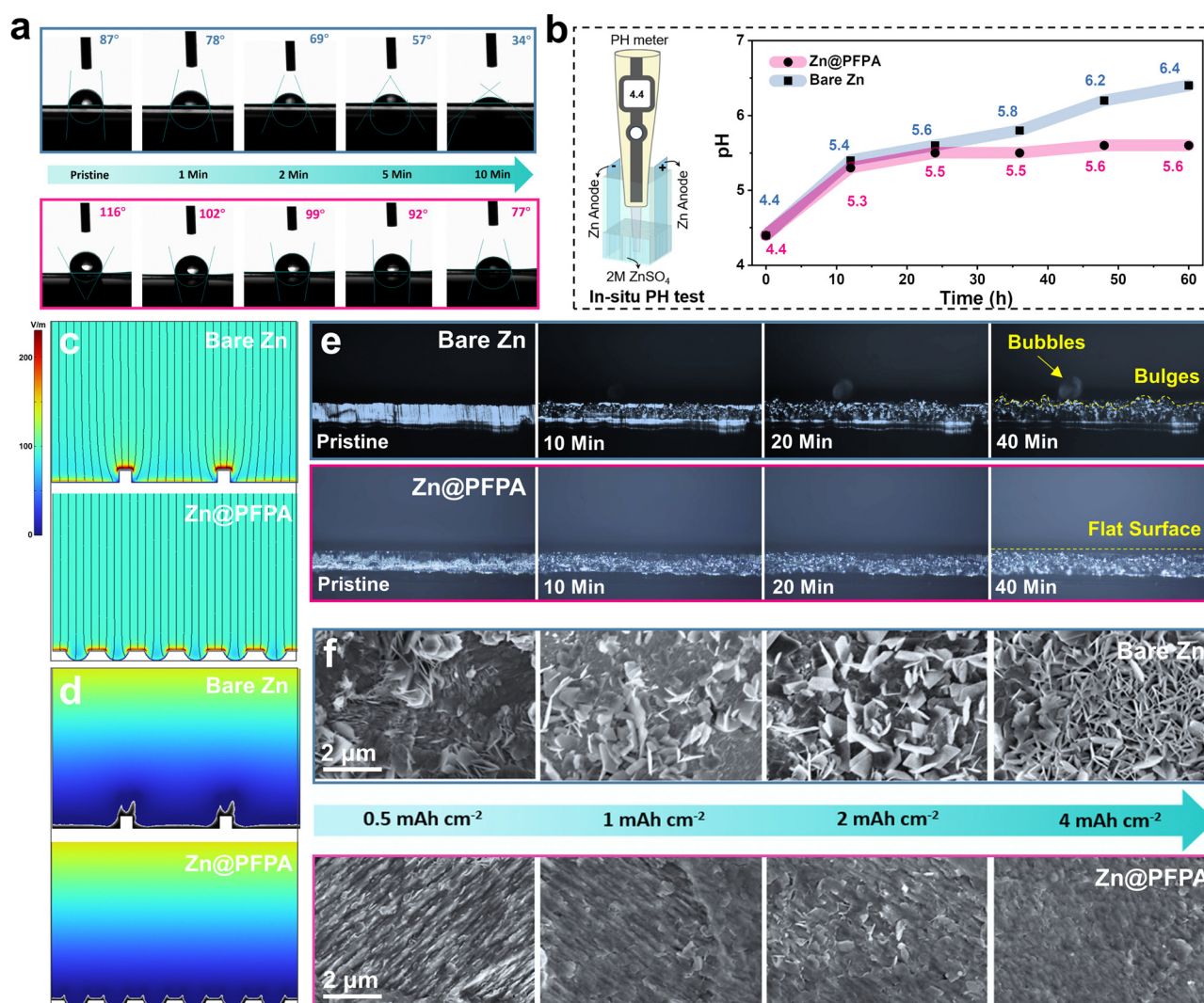

Fig. 4 The morphology and nature of bare Zn and Zn@PFPA during cycling. (a) Contact angle images at different times. (b) *In situ* pH test device and the variety of pH values during cycling. (c) and (d) COMSOL simulations of electric field distribution (c) and dendrites growth (d) for the surface of bare Zn and Zn@PFPA. (e) Visualization of the dendrites growth process at 10 mA cm^{-2}. (f) Deposition morphology at the different areal capacity.

This journal is © The Royal Society of Chemistry 2024

Energy Environ. Sci., 2024, **17**, 591–601 | **597**

The HER curves are tested with Na_2SO_4 electrolyte in Fig. S14b, ESI.† Due to the decrease of free H_2O on the interface, the HER is significantly suppressed with a higher overpotential on the Zn@PFPA interface compared with the bare Zn, corresponding to the result of the pH test. In this case, the related corrosion situation of the interface is investigated by the Tafel curves and displayed in Fig. S15a, ESI.† The Zn@PFPA electrode exhibits an anticorrosion interface, as evidenced by a significantly lower corrosion current (1.99 mA cm^{-2}) and potential (0.996 V) than that of the bare Zn electrode. To further confirm the excellent corrosion resistance performance of the Zn@PFPA electrode, the bare Zn and Zn@PFPA are soaked in the 2 M $ZnSO_2$ for 15 days (Fig. S15b, c, ESI†). The surface of bare Zn evidently forms substantial by-products due to the corrosion of the electrolyte. On the contrary, the Zn@PFPA presents flat surficial morphology, indicating desired anticorrosion properties. These results verify that the PFPA molecule withstands efficiently the invasion of H_2O and SO_4^{2-} and constructs a suppressed HER and anticorrosion interface.

The dendrite growth at the bare Zn and Zn@PFPA interfaces is examined from both experimental and theoretical perspectives. The surface of bare zinc possesses usually irregular bumps and veins caused by industrial machine production, which determines the non-uniform electric field during cycling, and thus promotes thriving dendrite growth.[45] As shown in Fig. 4c and d, the electric field strength and corresponding dendrites growth at the interface is calculated by COMSOL simulation. Bare zinc surfaces exhibit noticeable electric fields caused by uneven raised features or fluctuations, which result in the preferential growth of dendrites due to the more electrons gathered in those regions. After treatment by the PFPA, the bumps are substituted by the regular pattern that constructs an even electric field. As a result, the dendrite is prominently suppressed in the theoretical simulation. Additionally, uninterrupted and uniform Zn^{2+} flux is maintained by the PFPA molecules, which play an essential role in the non-dendric and reversible surface. *In situ* optical microscope is employed to visualize the growth situation of the dendrite (Fig. 4e). As the deposition progresses, the bare zinc surface gradually transitions from flat to forming disorganized bumps (Video S2, ESI†). In addition, significant bubble production can be seen during the deposition process, which is associated with severe HER on the bare zinc surface. However, the Zn@PFPA still maintains a relatively flat surface and no bubbles are detected in the same deposition time, suggesting the significant inhibition of dendrites and HER (Video S1, ESI†). The morphology of the surface during depositing is observed by scanning electron microscopy (SEM). As shown in Fig. 4f, at first only a few dendrites appear on the surface and the vertical unordered hexagonal dendrites are increasing with the deposition proceeding on the bare Zn surface due to the aggravation of the tip effect. These booming zinc dendrites will eventually puncture the separator and lead to a short circuit in the battery. In contrast to the disordered nature of bare zinc planes, the zinc metal on the Zn@PFPA surface is deposited in two-dimensional planes, forming a more orderly and structured arrangement. As deposition proceeds, the zinc metal grows still along the two-dimensional planes and gradually thickens.

Iodine cathodes feature high theoretical energy density and attractive voltage plateau.[46] However, the polyiodides (I^{3-} and I^{5-}), which are readily soluble in aqueous electrolytes, shuttles to the zinc anode surface causing corrosion and zinc dendrite growth. Such a zinc–iodine system brings about low CE, restricted rate capacity and stability, especially under high loading and high rate conditions.[47] Whereas the ultra-fast ionic transport and anti-corrosion interface consisting of PFPA molecules, the Zn@PFPA is considered to be suitable to address the challenges encountered in the zinc–iodine system (Fig. 5a). The I_2@C cathode is fabricated in this work by mixing the iodine and active carbon and the corresponding characterization is exhibited in Fig. S16, ESI.† The ESP calculation demonstrates that the PFPA molecules surrounded with negative charge prevent the approach of iodine anion and thus reduce the corrosion of the surface caused by the side reaction (Fig. 5b). The SEM images of bare Zn and Zn@PFPA electrodes after cycling are displayed in Fig. 5c and d. The bare Zn surface is corroded by electrolyte and iodine anions forming pits, which exacerbate the dendritic growth and the HER. Under the protection of the anticorrosion interface constructed by PFPA molecules, no significant corrosion and dendrites were observed at the Zn@PFPA electrode. In order to examine the self-discharge caused by the corrosion reaction ($Zn + I^{3-} \rightarrow Zn^{2+} + 3I^-$) on the electrodes, voltage-time curves after shelving were tested.[48] As exhibited in Fig. S17, ESI,† the bare Zn obtains a low reversible capacity with a CE of 84.9% after the shelving of 72 h, while the Zn@PFPA presents superior corrosion resistance, resulting in a higher CE of 90.0%.

The CV curves are performed at 0.5 mV s^{-1} (Fig. 5e). The voltage difference between the redox peaks represents the polarization of the battery. The Zn@PFPA electrode with a smaller voltage difference compared with bare Zn indicates that it has more rapid ion diffusion kinetics, which is caused by the ion self-expedited interface in the Zn@PFPA electrode. The same conclusion can be drawn in the impedance plots (Fig. S18, ESI†), in which the Zn@PFPA electrode has preponderant charge transfer resistance and Warburg impedance. In order to confirm the ultrafast ion transport capability of the Zn@PFPA electrode, the mass loading of the I_2@C cathode was increased to nearly 9 mg cm^{-2}. Rate performance is investigated with the I_2@C as cathode displayed in Fig. 5f and Fig. S19a, ESI.† Impressively, the Zn@PFPA-I_2@C battery achieves a superior rate capacity of 127 mA h g^{-1} even in the high current density of 10 A g^{-1}. The capacity decay of the Zn@PFPA electrode from 0.1 to 10 A g^{-1} is only 36.8%. Nevertheless, from 5 A g^{-1} onwards, the ions transfer rate of the bare Zn electrode cannot keep up with the fast current and occurs significant capacity decay, suggesting obvious capacity decay of 77% from 0.1 to 10 A g^{-1}. Moreover, the polarization voltage of two electrodes at different rates are compared in Fig. 5g and Fig. S19b, ESI.† The polarization of the two electrodes starts to differ significantly even at small current densities, and the difference is further widened as the current densities increase.
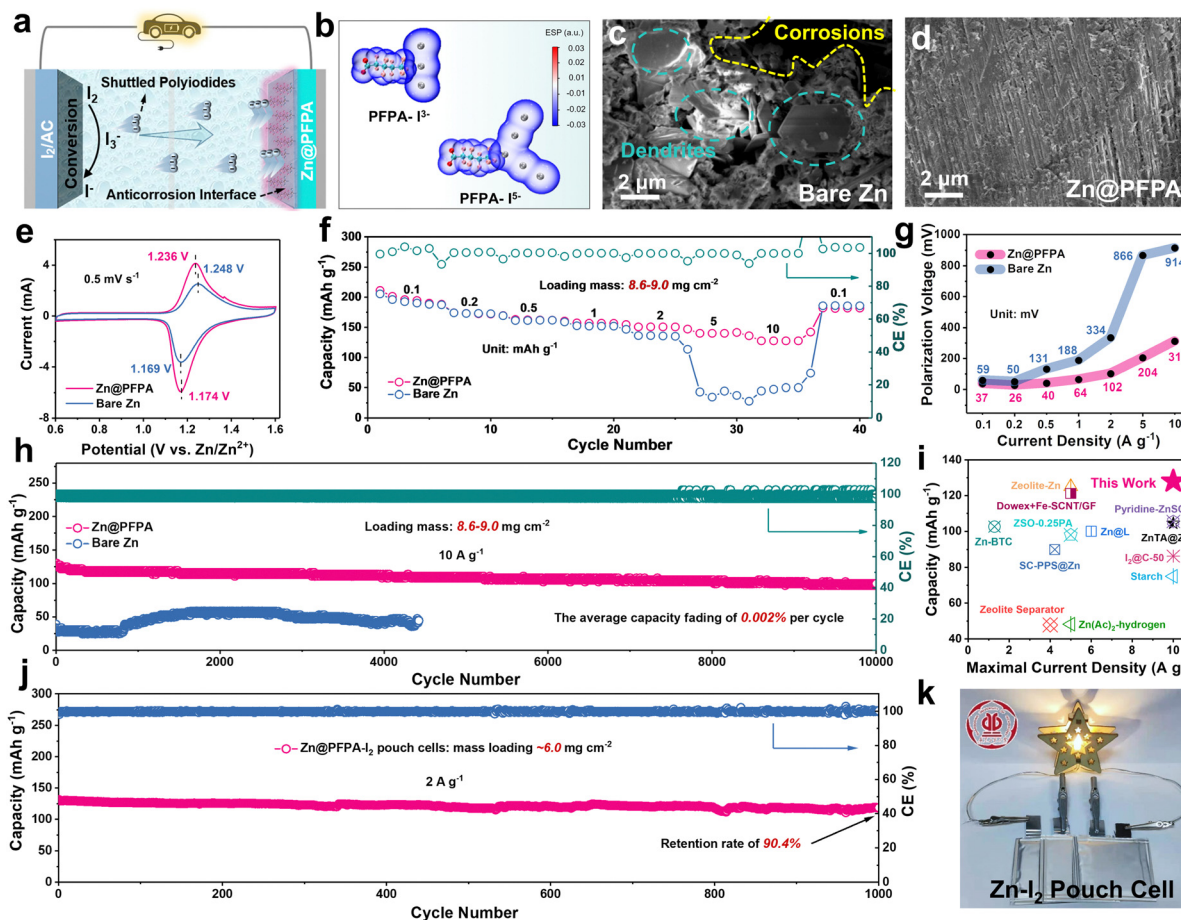
598 | *Energy Environ. Sci.*, 2024, **17**, 591–601

This journal is © The Royal Society of Chemistry 2024

Fig. 5 Electrochemical performance of high-rate and -loading Zn‖I₂@C full batteries. (a) The schematic diagram of the Zn@PFPA‖I₂@C systems. (b) EPS of the PFPA interacts with polyiodides. (c) and (d) SEM images of bare Zn (c) and Zn@PFPA (d) after charging/discharging. (e) CV curves at 0.5 mV s⁻¹. (f) Rate performance with high mass loading of 8.6–9 mg cm⁻². (g) The comparison of polarization voltage. (h) The cycling performance at 10 A g⁻¹ in a mass loading of 8.6–9 mg cm⁻². (i) The comparison with the published literature with respect to capacity at maximal current density. (j) The cycling performance of Zn@PFPA-I₂ pouch batteries at 2 A g⁻¹ in a mass loading of 6.2 mg cm⁻². (k) The luminous LED powered with three series-wound Zn−I₂ pouch cells.

Bare Zn electrode exhibits a steep polarization trend owing to the sluggish intrinsic kinetics, while Zn@PFPA achieves a significantly flatter polarization line. These results are attributed to that the participation of PFPA molecules in the desolvation process greatly accelerates the ion transport ability of the interface, and thus Zn@PFPA electrode withstands ultrafast current. The cycling stability also is evaluated at the harsh condition of 10 A g⁻¹ with the same mass loading of nearly 9 mg cm⁻², in which the outstanding lifespan of 10 000 cycles is achieved with an average capacity fading of 0.002% per cycle (Fig. 5h). The capacity at the maximal current density is compared with the relative literature reports published previously (Fig. 5i). The Zn@PFPA-I₂ battery is in an advantageous position by means of the remarkable capacity of 127 mA h g⁻¹ at 10 A g⁻¹.[44,46,49–58] To demonstrate the practical application capability, the relevant high-loading pouch batteries are also assembled. The Zn@PFPA-I₂ pouch battery endures stability of 1000 cycles at 2 A g⁻¹ with mass loading of I₂@C cathode of *ca.* 6.0 mg cm⁻² (Fig. 5j). In this case, a high-capacity retention of 90.4% is obtained. Three of these pouch batteries in series

can offer a voltage of 3.71 V and power the LEDs, indicating the potential practical application (Fig. 5k and Fig. S20, ESI†). Moreover, the outstanding performance is further verified by a more rigorous evaluation with thinner Zn@PFPA electrodes (10 and 20 μm) as the anode. In such conditions, the N/P ratio was also calculated based on the theoretical capacity (in the corresponding loading mass) of the anode and cathode. The Zn–I₂ batteries with the Zn@PFPA electrode thickness of 10 and 20 μm possess a low N/P ratio of 2.9 and 5.2, respectively. Nevertheless, Zn@PFPA electrodes still exhibit excellent rates and cycling performance. As shown in Fig. S21a, ESI,† a high-capacity retention of *ca.* 70% is achieved from 0.1 to 5 A g⁻¹. As expected, the Zn@PFPA electrodes endure 500 cycles, exhibiting the desired cycling performance (Fig. S21b, ESI†)

3. Conclusions

In summary, a dynamic and fast interfacial Zn²⁺ replenishment based on the Zn@PFPA layer is achieved to resist discontinuous

This journal is © The Royal Society of Chemistry 2024

Energy Environ. Sci., 2024, **17**, 591–601 | **599**

Zn^{2+} flux caused by the rapidly changed current at a high rate. This breakthrough is achieved through a unique mechanism of "self-expedited Zn^{2+} ion pump", where maintains a negatively charged interface resulting from the abundant C–F bonds and a high-activity area pattern. The PFPA saturated with negative charge participates in the solvation shell, significantly hastening the diffusion and desolvation processes of Zn^{2+}. Furthermore, this electronegative interface effectively repels anions and significantly reduces free H_2O molecules present at the interface. Therefore, at an ultrahigh current density of 50 mA cm^{-2}, the symmetric batteries with the Zn@PFPA electrode achieve an impressive lifespan of over 1900 h with a polarization potential of 2.6 times smaller than that of bare Zn. This accelerated ion transport, coupled with the enhanced anti-corrosion capabilities of the Zn@PFPA electrode bestows outstanding performance in Zn-I$_2$@C pouch batteries, presenting potential practical applications. This research provides valuable insights for the design and development of high-rate and multifunctional zinc anode interfaces.

Author contributions

S. H. conceived, designed and conducted the project and experiment. C. C. L. guided the experiments. Y. Y., X. L., Y. Z., Y. T., Z. W. and M. Y. assisted with the data analysis. R. T. performed the MD simulation and DFT calculation. S. H., Y. Y. and R. T. co-wrote the manuscript. All authors discussed the results and comments on the manuscript.

Conflicts of interest

The authors declare no conflict of interest.

Acknowledgements

Notes and references

1 J. Xiang, Y. Wei, Y. Zhong, Y. Yang, H. Cheng, L. Yuan, H. Xu and Y. Huang, *Adv. Mater.*, 2022, **34**, 2200912.

2 X. Jia, C. Liu, Z. G. Neale, J. Yang and G. Cao, *Chem. Rev.*, 2020, **120**, 7795–7866.

3 Z. Liu, Y. Huang, Y. Huang, Q. Yang, X. Li, Z. Huang and C. Zhi, *Chem. Soc. Rev.*, 2020, **49**, 180–232.

4 C. Yang, J. Xia, C. Cui, T. P. Pollard, J. Vatamanu, A. Faraone, J. A. Dura, M. Tyagi, A. Kattan, E. Thimsen, J. Xu, W. Song, E. Hu, X. Ji, S. Hou, X. Zhang, M. S. Ding, S. Hwang, D. Su, Y. Ren, X.-Q. Yang, H. Wang, O. Borodin and C. Wang, *Nat. Sustainability*, 2023, **6**, 325–335.

5 D. Han, C. Cui, K. Zhang, Z. Wang, J. Gao, Y. Guo, Z. Zhang, S. Wu, L. Yin, Z. Weng, F. Kang and Q.-H. Yang, *Nat. Sustainability*, 2021, **5**, 205–213.

6 C. Li, S. Jin, L. A. Archer and L. F. Nazar, *Joule*, 2022, **6**, 1733–1738.

7 F. Wang, L. E. Blanc, Q. Li, A. Faraone, X. Ji, H. H. Chen-Mayer, R. L. Paul, J. A. Dura, E. Hu, K. Xu, L. F. Nazar and C. Wang, *Adv. Energy Mater.*, 2021, **11**, 2102016.

8 J. He, Y. Tang, G. Liu, H. Li, M. Ye, Y. Zhang, Q. Yang, X. Liu and C. Li, *Adv. Energy Mater.*, 2022, **12**, 2202661.

9 S. Zheng, L. Wei, Z. Zhang, J. Pan, J. He, L. Gao and C. C. Li, *Nano Lett.*, 2022, **22**, 9062–9070.

10 D. Wang, D. Lv, H. Liu, S. Zhang, C. Wang, C. Wang, J. Yang and Y. Qian, *Angew. Chem., Int. Ed.*, 2022, **61**, e202212839.

11 X. Xie, S. Liang, J. Gao, S. Guo, J. Guo, C. Wang, G. Xu, X. Wu, G. Chen and J. Zhou, *Energy Environ. Sci.*, 2020, **13**, 503–510.

12 L. Qian, H. Zhu, T. Qin, R. Yao, J. Zhao, F. Kang and C. Yang, *Adv. Funct. Mater.*, 2023, **33**, 2301118.

13 Y. Yang, H. Hua, Z. Lv, W. Meng, M. Zhang, H. Li, P. Lin, J. Yang, G. Chen, Y. Kang, Z. Wen, J. Zhao and C. C. Li, *ACS Energy Lett.*, 2023, **8**, 1959–1968.

14 F. Wang, H. Lu, H. Zhu, L. Wang, Z. Chen, C. Yang and Q.-H. Yang, *Energy Storage Mater.*, 2023, **58**, 215–221.

15 M. Zhao, J. Rong, F. Huo, Y. Lv, B. Yue, Y. Xiao, Y. Chen, G. Hou, J. Qiu and S. Chen, *Adv. Mater.*, 2022, **34**, 2203153.

16 Y. Guo, W. Cai, Y. Lin, Y. Zhang, S. Luo, K. Huang, H. Wu and Y. Zhang, *Energy Storage Mater.*, 2022, **50**, 580–588.

17 Y. Mu, Z. Li, B.-K. Wu, H. Huang, F. Wu, Y. Chu, L. Zou, M. Yang, J. He, L. Ye, M. Han, T. Zhao and L. Zeng, *Nat. Commun.*, 2023, **14**, 4205.

18 Z. Xu, S. Jin, N. Zhang, W. Deng, M. H. Seo and X. Wang, *Nano Lett.*, 2022, **22**, 1350–1357.

19 Y. Gao, Q. Cao, J. Pu, X. Zhao, G. Fu, J. Chen, Y. Wang and C. Guan, *Adv. Mater.*, 2022, **35**, 2207573.

20 Q. Cao, Y. Gao, J. Pu, X. Zhao, Y. Wang, J. Chen and C. Guan, *Nat. Commun.*, 2023, **14**, 641.

21 G. Zhang, X. Zhang, H. Liu, J. Li, Y. Chen and H. Duan, *Adv. Energy Mater.*, 2021, **11**, 2003927.

22 H. Liu, J. Li, X. Zhang, X. Liu, Y. Yan, F. Chen, G. Zhang and H. Duan, *Adv. Funct. Mater.*, 2021, **31**, 2106550.

23 Z. Yi, G. Chen, F. Hou, L. Wang and J. Liang, *Adv. Energy Mater.*, 2021, **11**, 2003065.

24 J. Zhou, F. Wu, Y. Mei, Y. Hao, L. Li, M. Xie and R. Chen, *Adv. Mater.*, 2022, **34**, 2200782.

25 W. Du, E. H. Ang, Y. Yang, Y. Zhang, M. Ye and C. C. Li, *Energy Environ. Sci.*, 2020, **13**, 3330–3360.

26 J. Hao, X. Li, X. Zeng, D. Li, J. Mao and Z. Guo, *Energy Environ. Sci.*, 2020, **13**, 3917–3949.

600 | *Energy Environ. Sci.*, 2024, **17**, 591–601

This journal is © The Royal Society of Chemistry 2024

27 X.-R. Chen, Y.-X. Yao, C. Yan, R. Zhang, X.-B. Cheng and Q. Zhang, *Angew. Chem., Int. Ed.*, 2020, **59**, 7743–7747.

28 Z. Liu, L. Li, L. Qin, S. Guo, G. Fang, Z. Luo and S. Liang, *Adv. Mater.*, 2022, **34**, 2204681.

29 Y. Fan, S. Li, X. Tao, Y. Wang, Z. Liu, H. Chen, Z. Wu, J. Zhang, F. Ren, X. Chen and E. Fu, *Nano Energy*, 2021, **90**, 106574.

30 L. Hong, X. Wu, L.-Y. Wang, M. Zhong, P. Zhang, L. Jiang, W. Huang, Y. Wang, K.-X. Wang and J.-S. Chen, *ACS Nano*, 2022, **16**, 6906–6915.

31 Y. Xie, Y. Huang, Y. Zhang, T. Wu, S. Liu, M. Sun, B. Lee, Z. Lin, H. Chen, P. Dai, Z. Huang, J. Yang, C. Shi, D. Wu, L. Huang, Y. Hua, C. Wang and S. Sun, *Nat. Commun.*, 2023, **14**, 2883.

32 S. Tao, C. Zhang, J. Zhang, Y. Jiao, M. Li, W. Lin, L. Ran, B. Clement, M. Lyu, I. Gentle, L. Wang and R. Knibbe, *Chem. Eng. J.*, 2022, **446**, 136607.

33 P. Wang, S. Liang, C. Chen, X. Xie, J. Chen, Z. Liu, Y. Tang, B. Lu and J. Zhou, *Adv. Mater.*, 2022, **34**, 2202733.

34 M. Li, Z. Li, X. Wang, J. Meng, X. Liu, B. Wu, C. Han and L. Mai, *Energy Environ. Sci.*, 2021, **14**, 3796–3839.

35 Y. Yang, H. Hua, Z. Lv, M. Zhang, C. Liu, Z. Wen, H. Xie, W. He, J. Zhao and C. C. Li, *Adv. Funct. Mater.*, 2022, **33**, 2212446.

36 H. Liu, J.-G. Wang, W. Hua, L. Ren, H. Sun, Z. Hou, Y. Huyan, Y. Cao, C. Wei and F. Kang, *Energy Environ. Sci.*, 2022, **15**, 1872–1881.

37 H. Peng, Y. Fang, J. Wang, P. Ruan, Y. Tang, B. Lu, X. Cao, S. Liang and J. Zhou, *Matter*, 2022, **5**, 4363–4378.

38 Y. Cui, Q. Zhao, X. Wu, X. Chen, J. Yang, Y. Wang, R. Qin, S. Ding, Y. Song, J. Wu, K. Yang, Z. Wang, Z. Mei, Z. Song, H. Wu, Z. Jiang, G. Qian, L. Yang and F. Pan, *Angew. Chem., Int. Ed.*, 2020, **59**, 16594–16601.

39 P. Chen, X. Yuan, Y. Xia, Y. Zhang, L. Fu, L. Liu, N. Yu, Q. Huang, B. Wang, X. Hu, Y. Wu and T. van Ree, *Adv. Sci.*, 2021, **8**, 2100309.

40 C. Liu, Z. Li, X. Zhang, W. Xu, W. Chen, K. Zhao, Y. Wang, S. Hong, Q. Wu, M.-C. Li and C. Mei, *Adv. Sci.*, 2022, **9**, 2202380.

41 X. Zeng, K. Xie, S. Liu, S. Zhang, J. Hao, J. Liu, W. K. Pang, J. Liu, P. Rao, Q. Wang, J. Mao and Z. Guo, *Energy Environ. Sci.*, 2021, **14**, 5947–5957.

42 J. Zheng, Z. Cao, F. Ming, H. Liang, Z. Qi, W. Liu, C. Xia, C. Chen, L. Cavallo, Z. Wang and H. N. Alshareef, *ACS Energy Lett.*, 2022, **7**, 197–203.

43 Z. Wu, M. Li, Y. Tian, H. Chen, S.-J. Zhang, C. Sun, C. Li, M. Kiefel, C. Lai, Z. Lin and S. Zhang, *Nano-Micro Lett.*, 2022, **14**, 110.

44 Y. Kang, G. Chen, H. Hua, M. Zhang, J. Yang, P. Lin, H. Yang, Z. Lv, Q. Wu, J. Zhao and Y. Yang, *Angew. Chem., Int. Ed.*, 2023, **62**, e202300418.

45 S. Zhang, M. Ye, Y. Zhang, Y. Tang, X. Liu and C. C. Li, *Adv. Funct. Mater.*, 2023, **33**, 2208230.

46 Y. Lyu, J. A. Yuwono, P. Wang, Y. Wang, F. Yang, S. Liu, S. Zhang, B. Wang, K. Davey, J. Mao and Z. Guo, *Angew. Chem., Int. Ed.*, 2023, **62**, e202303011.

47 G. Liang, J. Zhu, B. Yan, Q. Li, A. Chen, Z. Chen, X. Wang, B. Xiong, J. Fan, J. Xu and C. Zhi, *Energy Environ. Sci.*, 2022, **15**, 1086–1096.

48 Y. Zong, H. He, Y. Wang, M. Wu, X. Ren, Z. Bai, N. Wang, X. Ning and S. X. Dou, *Adv. Energy Mater.*, 2023, **13**, 2300403.

49 L. Zhang, J. Huang, H. Guo, L. Ge, Z. Tian, M. Zhang, J. Wang, G. He, T. Liu, J. Hofkens, D. J. L. Brett and F. Lai, *Adv. Energy Mater.*, 2023, **13**, 2203790.

50 H. Yang, Y. Qiao, Z. Chang, H. Deng, P. He and H. Zhou, *Adv. Mater.*, 2020, **32**, 2004240.

51 W. Shang, Q. Li, F. Jiang, B. Huang, J. Song, S. Yun, X. Liu, H. Kimura, J. Liu and L. Kang, *Nano-Micro Lett.*, 2022, **14**, 82.

52 P.-F. Zhang, Z. Wu, S.-J. Zhang, L.-Y. Liu, Y. Tian, Y. Dou, Z. Lin and S. Zhang, *Nano Energy*, 2022, **102**, 107721.

53 Z. Li, X. Wu, X. Yu, S. Zhou, Y. Qiao, H. Zhou and S.-G. Sun, *Nano Lett.*, 2022, **22**, 2538–2546.

54 W. Shang, J. Zhu, Y. Liu, L. Kang, S. Liu, B. Huang, J. Song, X. Li, F. Jiang, W. Du, Y. Gao and H. Luo, *ACS Appl. Mater. Interfaces*, 2021, **13**, 24756–24764.

55 K. Wang, J.-B. Le, S.-J. Zhang, W.-F. Ren, J.-M. Yuan, T.-T. Su, B.-Y. Chi, C.-Y. Shao and R.-C. Sun, *J. Mater. Chem. A*, 2022, **10**, 4845–4857.

56 Y. Chen, F. Gong, W. Deng, H. Zhang and X. Wang, *Energy Storage Mater.*, 2023, **58**, 20–29.

57 S.-J. Zhang, J. Hao, H. Li, P.-F. Zhang, Z.-W. Yin, Y.-Y. Li, B. Zhang, Z. Lin and S.-Z. Qiao, *Adv. Mater.*, 2022, **34**, 2201716.

58 W. Li, K. Wang and K. Jiang, *J. Mater. Chem. A*, 2020, **8**, 3785–3794.

This journal is © The Royal Society of Chemistry 2024

Energy Environ. Sci., 2024, **17**, 591–601 | **601**